Energy & Environmental Science

Accepted Manuscript

ROYAL SOCIETY OF CHEMISTRY

www.rsc.org/ees

Journal Name

RSCPublishing

COMMUNICATION

CO_2-free electric power circulation via direct charge and discharge using the glycolic acid/oxalic acid redox couple

Cite this: DOI: 10.1039/x0xx00000x

Received 00th January 2012,
Accepted 00th January 2012

DOI: 10.1039/x0xx00000x

www.rsc.org/

R. Watanabe,[ab] M. Yamauchi,[*ab] M. Sadakiyo,[ab] R. Abe[bc] and T. Takeguchi[bd]

The establishment of an efficient electric power distribution method is the key to realising a sustainable society driven by renewable-energy-based electricity, such as solar photovoltaic, wind turbine, and wave electricity, in view of supply instability. Here, we demonstrate an electric power circulation method that does not emit CO_2 and is based on the glycolic acid (GC)/oxalic acid (OX) redox couple. Direct electric power storage in GC ensures considerable high energy density storage and good transportability through OX electroreduction with significantly high selectivity (>98%) using pure anatase-type titania (TiO_2) spheres under mild conditions in the potential region of -0.5 to -0.7 V vs. the RHE at 50 ºC. The most desirable characteristic of this electroreduction is the suppression of hydrogen evolution even in acidic aqueous media (Faraday efficiency of 70–95%, pH 2.1). We also successfully generated power without CO_2 emissions via selective electrooxidation of GC with an alkaline fuel cell.

Efficient energy storage via the conversion of electric power into high-energy chemicals, so-called energy carriers, is critically important for the practical application of intermittent renewable energies[1-3]. Hydrogen is a clean energy carrier that is producible by water electrolysis using renewable electricity[4-6] and does not produce any harmful wastes or CO_2 in the power generation process[6]. The development of efficient hydrogen storage and release systems remains a challenge for long-distance transportation and long-term storage[7,8] because hydrogen is gaseous and highly explosive (13 MJ/m^3 energy density and 4-74% flammability limits in air[9]). Recently, methods for the highly efficient storage of hydrogen by compression[10], liquefaction[7], adsorption using porous materials such as zeolites[11], carbon materials[12] and metal-organic frameworks[13], and chemical storage using cyclic hydrocarbons[14], formic acid[15] and inorganic hydrides[16,17] have reached an advanced stage. Gas storage and release operations entail a certain loss of energy efficiency, increasing the energy costs of energy circulation using hydrogen, as described in Scheme S1.

Alcohols have been regarded as an energy carrier because of their considerably high energy density (e.g., energy densities of ethanol and ethylene glycol are 23,000 and 22,000 MJ/m^3, respectively) and appropriate chemical stability. The direct electrooxidation of alcohols in fuel cells has been widely investigated[18,19]. The perfect oxidation of alcoholic compounds, however, results in CO_2 emissions as long as carbon-containing chemicals are used as a fuel. On the other hand, the partial oxidation of alcohols into carboxylic acids generates ca. 80 % of potentially available electric power without CO_2 emission[20], as described in equation (1).

$$R\text{-}CH_2OH + H_2O \rightarrow R\text{-}COOH + 4H^+ + 4e^- \quad (1)$$

Furthermore, if alcoholic chemicals are directly renewed by the electroreduction of the carboxylic acids using renewable electricity, in accordance with the reverse reaction of equation (1), we can sustainably circulate renewable energy through the intermediary of an alcohol/carboxylic acid redox couple. Recently, we have reported power generation by the partial electrooxidation of ethylene glycol, which is easily handled, into oxalic acid (HOOC-COOH, **OX**) without CO_2 emission[20]. Renewing alcoholic compounds by direct electroreduction of **OX** is another challenge, which enables highly efficient electric power circulation. To the best of our knowledge, the electroreduction of carboxylic acids to alcoholic compounds has never been achieved. Meanwhile, the chemical reduction of carboxylic acids into alcoholic chemicals is an in-demand chemistry in fine chemical production[21-24] and bio-refineries[25-30]. Considering that alcohol productions from carboxylic acids have been conducted

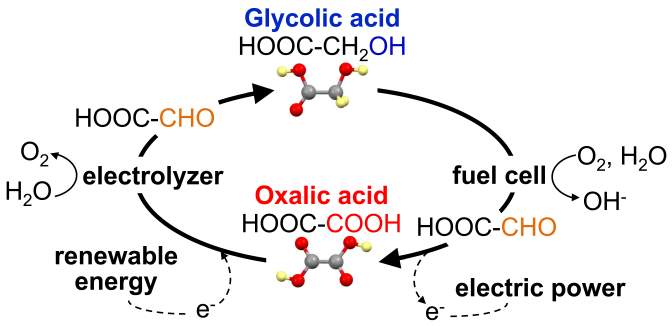

Scheme 1 Carbon-neutral energy cycling using the **GC**/**OX** redox couple. Grey, red and yellow spheres represent carbon, oxygen and hydrogen atoms, respectively.

under severe conditions (e.g., 100-380 ºC, 2-6 MPa of hydrogen atmosphere)[23-27], development of efficient carboxylic acid reduction catalysts is expected to open up novel synthetic routes for useful chemical products. Then, we surveyed the catalytic performances of various metals and oxides, including Al, Ti, V, Ni, Cu, Zr, Nb, Mo, Sn, Pt and Pb, and determined that only calcined Ti foil catalyses the electrochemical reduction of **OX** to 2-electron-reduced glyoxylic acid (HOOC-CHO, GO) and a small amount of 4-electron-reduced glycolic acid (HOOC-CH_2OH, **GC**) (Fig. S1). Several compounds are considerable as a reduced form of **OX** via multistep reductions as shown in Scheme S2. However, only GO and **GC** were obtained in the electrorediction on the Ti foil. The catalytic activity was enhanced by the calcination of the Ti foil, with observed product yields on Ti and calcined Ti of 0.3 and 2.9%, respectively. This activity presumably indicates that a TiO_2 layer that formed on the Ti foil acted as an active site for **OX** reduction.

The fabrication of nanostructures as electrocatalysts contributes to the enhancement of catalytic performance by maximising the availability of catalytic sites and facilitating the diffusion of electrons and reactants by increasing the catalyst's surface area[31,32]. We aimed to further increase the **OX** reduction activity to increase selectivity for the highly reduced **GC** by increasing the active surfaces of the TiO_2 by synthesising nanometre-sized TiO_2 as porous TiO_2 spheres (**PTS**s) with a high specific surface area using layered protonated titanate (LPT) calcination[33]. In this paper, we demonstrate the highly selective and efficient electroreduction of **OX** to **GC** using purely anatase-type **PTS**s under moderate conditions in the potential region of -0.5 to -0.7 V vs. the reversible hydrogen electrode (RHE). **GC** is chemically stable and has a high energy density (8,600 and 13,000 MJ/m^3 for partial and perfect oxidations, to **OX** and CO_2 respectively), which are similar to the densities of ethanol in the case of partial oxidation to acetic acid (8,400 MJ/m^3). The most distinguishable merit of using the alcohol/carboxylic acid redox couple as an energy carrier is the facilitation of storage and release operations compared to gaseous carrier systems, leading to an improvement in the energy efficiency, as described in Scheme S1. Furthermore, we succeeded in directly generating power from **GC** using an alkaline fuel cell without CO_2 emission. Briefly, this paper represents the first demonstration of carbon-neutral energy circulation by direct electric power charge/discharge using energy carriers (Scheme 1).

PTSs were synthesised by calcination of LPT at 150, 300, 450, 500, 525, 550 and 600 ºC for 1 h under flowing air[33]. The LPT and the **PTS**s were characterised by X-ray diffraction (XRD), transmission electron microscopy (TEM) and nitrogen adsorption-desorption measurements. XRD patterns of uncalcined and calcined LPTs are shown in Figs. S2(a) and (b). The XRD pattern of the uncalcined LPT is assignable to the $H_2Ti_2O_5 \cdot H_2O$ phase. However,

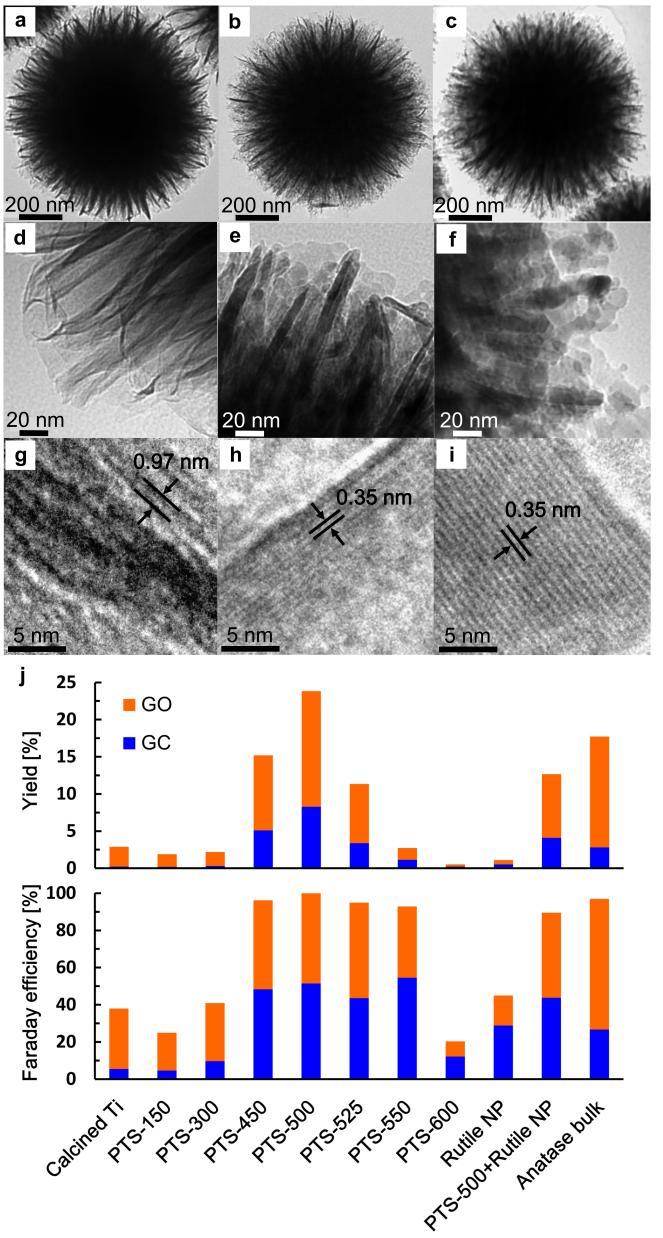

Fig. 1 (a-i) TEM images of layered protonated titanate (LPT) before and after calcination. Low-magnification (top), high-magnification (middle) and high-resolution images (bottom) of LPT (a, d and g) and LPT calcined at 500 (**PTS**-500, b, e and, h) and 600 ºC (**PTS**-600, c, f and, i). **OX** electroreduction performances of a variety of TiO_2 catalysts. (j) Yields and Faraday efficiencies for products generated in **OX** electroreductions using calcined Ti foil and **PTS**s, rutile NP, a physical mixture of **PTS**-500 and rutile NP, and anatase bulk deposited onto Ti foil. Orange and blue bars represent yields and Faraday efficiencies of **GC** and GO generations, respectively. The **OX** electroreductions were performed at -0.627 V vs. RHE at 24 ºC for 2 h in 0.16 M **OX** solution containing 0.16 M Na_2SO_4 (pH 1.2).

the peaks in the diffraction pattern of the LPTs calcined at 150 ºC were attributable to an anatase-type TiO_2 phase in addition to those from the $H_2Ti_2O_5 \cdot H_2O$ phase, and the diffraction intensities from the anatase phase increased with increasing calcination temperature. Only XRD patterns of anatase-type TiO_2 were obtained from LPT calcined at temperatures above 500 ºC (Figs. S2(a), (b) and (c)).

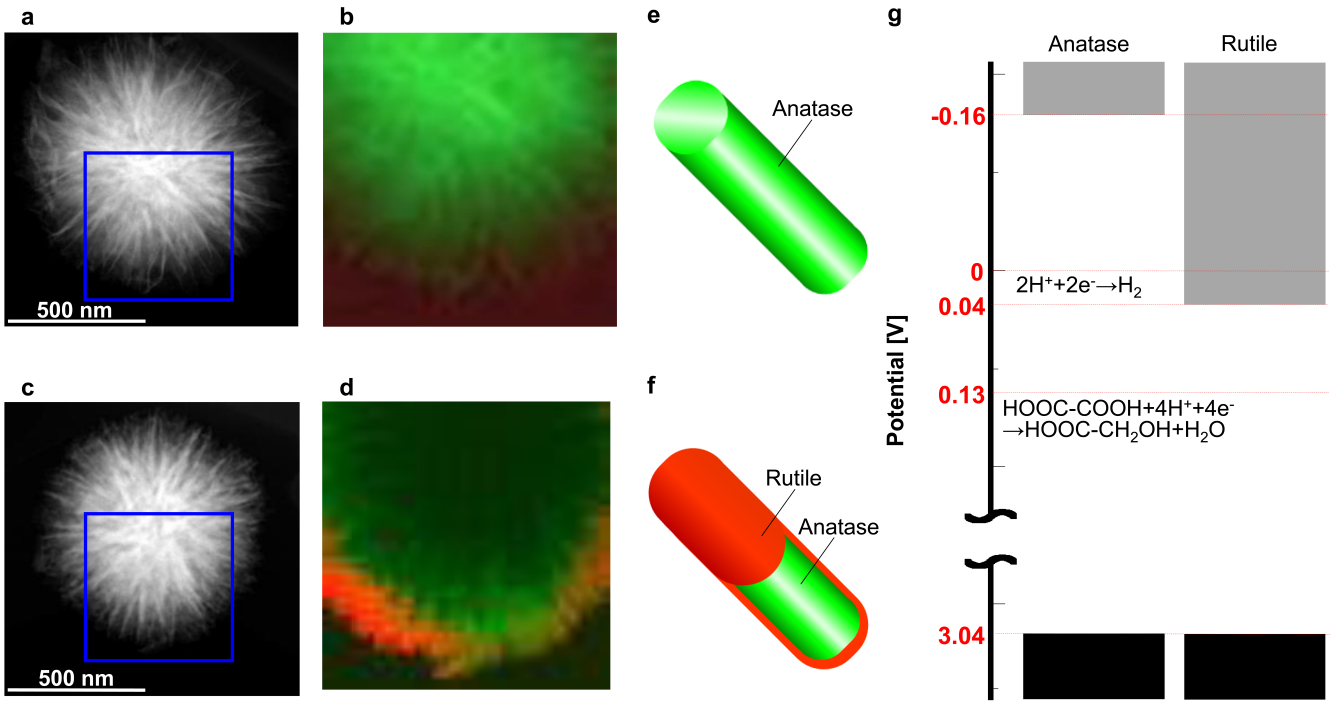

Fig. 2 EELS maps of anatase and rutile phases on **PTS**s and energy diagrams of anatase- and rutile-type TiO_2 included in **PTS**s. (a) and (c) STEM images of **PTS**-500 and -600. (b) and (d) EELS maps of **PTS**-500 and -600 composed of Ti L_3-edge signals in the area marked by red squares in (a) and (c). The EELS signal intensities from the anatase and rutile phases are recognised by green and red colours, respectively. The dark area in **PTS**-600 shown in (d) indicates the weakened intensity of the beam caused by transmission through the thick centre of **PTS**-600. Illustrations for distributions of anatase and rutile phases in (e) **PTS**-500 and (f) **PTS**-600. (g) Energy diagrams of conduction and valence bands for anatase- and rutile-type TiO_2 conduction and valence bands and redox potentials for H_2 and **GC** evolutions. The grey and black squares represent conduction and valence bands, respectively, assuming that the flat-band potential is equal to the conduction-band edge potential.

TEM revealed that all of the calcined LPTs exhibited spherical morphologies, irrespective of the calcination temperature, with sizes ranging from 800 to 1,100 nm (Figs. 1(a), (b) and (c) and Figs. S3(a), (b), (c), (d) and (i)). The calcined LPTs are denoted together with their calcination temperatures as **PTS**-150, -300, -450, -500, -525, -550 and -600. High-magnification TEM images of the products are shown in Figs. 1(d), (e) and (f) and in Figs. S3(e), (f), (g) and (h). We observed that an LPT was constructed from a number of thin nanosheets. As the calcination temperature increased, the nanosheets gradually converted into nanorod-like morphologies with a high aspect ratio of 5-15 nm × 400-500 nm. When the calcination temperature was increased to 600 ºC, the rod-like morphologies partially crumbled. High-resolution (HR) TEM observations provided more detailed structural information. An observed interlayer distance of 0.97 nm in the layered structure of the LPTs was assignable to the (002) planes of $H_2Ti_2O_5{\cdot}H_2O$, and the measured *d*-spacing of 0.35 nm for the nanorods contained in **PTS**-500 and -600 fitted the (101) spacing of anatase-type TiO_2 (Figs. 1(g), (h) and (i)). These characterisations indicated that the structural features, crystallinity and surface morphology varied with the calcination temperature and that **PTS**s prepared at calcination temperatures higher than 500 ºC were composed primarily of a highly crystalline anatase-type TiO_2 phase (>99 wt.%) and characterised by a large surface area (82.1-43.2 m^2/g) (Figs. S2(c) and (d), and 3(j), (k) and (l)).

The catalytic activity of **PTS**s in **OX** electroreduction was examined by chronoamperometry (CA) in 0.16 M **OX** with 0.16 M Na_2SO_4 at -0.627 V vs. RHE at 24 ºC. Electrodes were prepared by drying a methanol **PTS** suspension dropped onto Ti foil, followed by calcination at 150-600 ºC. As summarised in Fig. 1(j), the product yield and Faraday efficiency of the **PTS** deposited Ti foil electrodes increased with increasing calcination temperature up to 500 ºC, i.e., the highest product yield (23.8%) was attained with **PTS**-500, which was easily correlated to the structural change from $H_2Ti_2O_5{\cdot}H_2O$ to the catalytically active TiO_2 phase with increasing temperature. Notably, the **OX** electroreduction on **PTS**-500 proceeded with 34.7% **GC** selectivity and 100% Faraday efficiency. However, the product yield and Faraday efficiency on the electrode treated above 500 ºC sharply deteriorated, with the **PTS**-600-mounted electrode demonstrating a minimal product yield (0.5%), although the **PTS** structures should have been nearly unchanged according to our XRD analyses. To understand this rapid catalytic deterioration, we examined the surface states of active **PTS**-500 and inactive **PTS**-600 by X-ray photoelectron spectroscopy (XPS) (Figs. S4(a), (b), (c) and (d)). The O 1s peaks were recorded at approximately 527-533 eV for both **PTS**s and could be decomposed into two spectral components assignable to the surface hydroxyl group and the structural oxygen in TiO_2[34] (Figs. S4(c) and (d)). The peak area ratios (A_{TiO2}/A_{OH}) for the structural oxygen (A_{TiO2}) and hydroxyl oxygen species (A_{TiO2}) on **PTS**-500 and -600 were calculated to be 0.206 and 0.110, respectively. The disagreement in these values seems reasonable given that the different surface areas of the **PTS**s, i.e., the A_{TiO2}/A_{OH} values normalised by the BET surface area of **PTS**-500 and -600 (Fig. S3(l)), were calculated to be 2.51×10^{-3} and 2.54×10^{-3}, respectively, which are almost identical. Furthermore, we confirmed no **OX** affinity difference between the two types of **PTS**s using classical adsorption measurements (Fig. S4(e)). These results imply that the difference in catalytic activity between **PTS**-500 and -600

originates from their interior aspects. Ultraviolet-visible (UV-Vis) absorption spectroscopic characterisation of **PTS**-500, -550, -600 and rutile-type TiO_2 nanoparticles (rutile NPs, Fig. S5) showed that sharp increases in absorption in the wavelength region of λ = 390-410 nm corresponded to the band-gap energy of TiO_2 (Fig. S6(a)). The observed redshifts with increasing calcination temperature are explained by the gradual structural change from the anatase to the rutile phase, although a negligible amount of rutile phase formation was confirmed in inactive **PTS**-600. These results correlate the catalytic degradation and rutile phase formation, indicating the significance of detailed surface structure analyses for further mechanistic understanding. Anatase- and rutile-type TiO_2 show characteristic electron energy-loss spectral (EELS) patterns[35] (Figs. S6(b) and (c)), respectively. We produced scanning TEM (STEM) images and phase distribution maps of the anatase and rutile phases on **PTS**-500 and -600 via the spectral structure recognition of each phase, as shown in Figs. 2(a), (b), (c) and (d). Interestingly, EELS mapping revealed that **PTS**-500 is composed of purely anatase-type TiO_2, whereas **PTS**-600 contains a rutile-type TiO_2, especially around the surface. We examined the catalytic activity of rutile NPs, which are characterised by a different crystal symmetry, and observed that both product yield and Faraday efficiency on rutile NP were relatively low compared to those on **PTS**-500 (Fig. 1(j)). In addition, we observed that the catalytic performance of a 1:1 physical mixture of **PTS**-500 and rutile NP was considerably higher than that of **PTS**-600 (Fig. 1(j)). Thus, the excellent catalytic activity of **PTS**-500 can be attributed to catalyst surface composed of only of anatase phase. The drastic decrease in the catalytic performance on **PTS**-600 originated from the formation of the rutile-type TiO_2 thin layer that was closely attached to the anatase-type TiO_2 spheres by calcination above 500 ºC as illustrated in Figs. 2(e) and (f).

Here, we discuss why **PTS**-500 serves as a highly efficient and selective electrocatalyst to convert **OX** into **GC**. The conduction-band bottom of anatase-type TiO_2 lies at a position that is 0.2 V higher than that of rutile-type TiO_2[36], resulting in the greater reducibility of anatase-type TiO_2 compared to rutile-type TiO_2 (Fig. 2(g)). Electrons provided by the electrode are possibly accumulated in the conduction band of TiO_2. Therefore, electrons introduced into the conduction band of anatase-type TiO_2 have a higher reduction potential than those introduced into the conduction band of rutile-type TiO_2. In aqueous media, H_2 evolution can be a major reaction due to the high collision probabilities of protons with catalysts, especially under acidic conditions. Nevertheless, **GC** formation occurs over the **PTS**s with 100% Faraday efficiency, most likely assignable to the formation of oxygen vacancies at bridging sites and to the conversion of Ti^{4+} sites to Ti^{3+} sites during the application of electric current. The Ti^{3+} sites are stable under acidic conditions[37-39] and are favourable for the adsorption of a hydrophilic carboxyl group in a manner similar to the behaviour of the photogenerated hydrophilicity of TiO_2[40], leading to the high Faraday efficiency for **OX** reduction, i.e., suppression of hydrogen evolution. To evaluate the effects of the porous morphology of **PTS**s on catalytic activity, nonporous, bulky, anatase-type TiO_2 (anatase bulk) with a specific surface area of 10.1 m^2/g was synthesised and used as a catalyst (Fig. S7). The anatase bulk exhibited smaller product yield and lower **GC** selectivity than **PTS**-500, indicating that the high **PTS** surface area favours efficient **OX** reduction (Fig. 1(j)).

We next conducted detailed studies on **OX** reduction using **PTS**s.

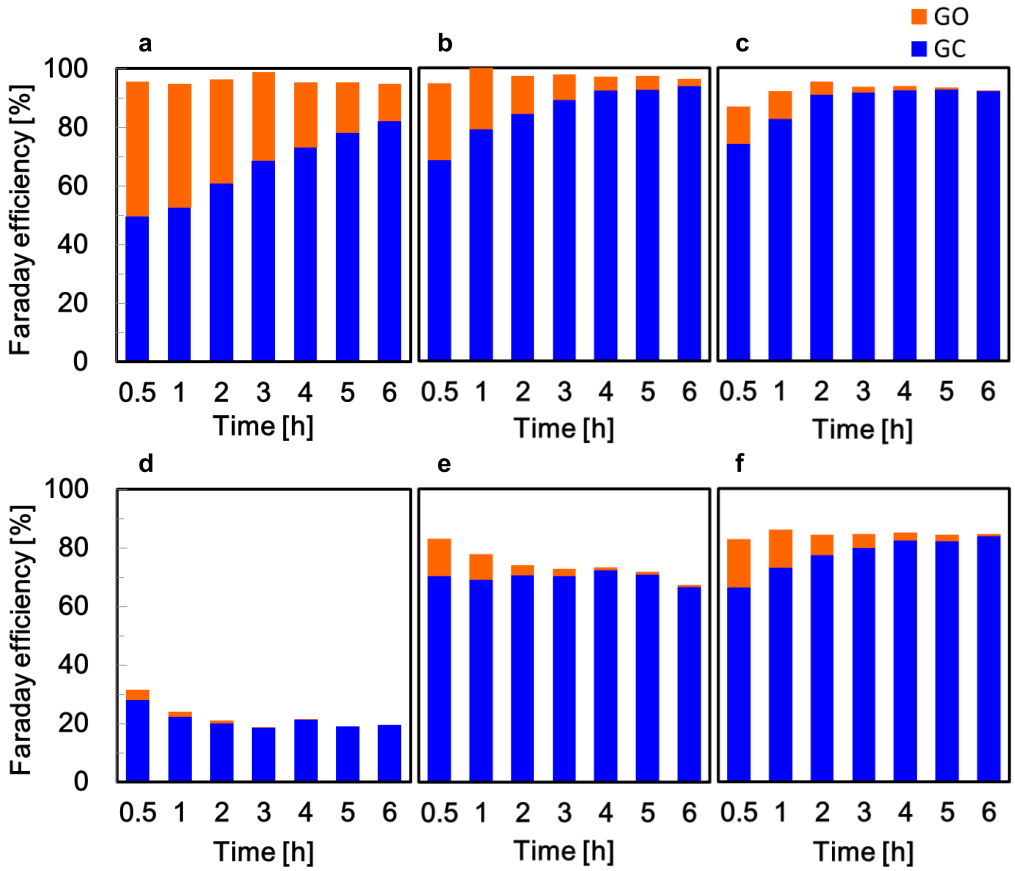

Fig. 3 Catalytic performance of **PTS**-500 at various temperatures and potentials. Faraday efficiencies for the formation of reduction products generated at -0.7 V vs. RHE and (a) 24, (b) 40, and (c) 50 ºC and at (d) -0.4, (e) -0.5, and (f) -0.6 V vs. RHE. All electrochemical experiments, except for the blank measurement, were conducted in 0.03 M **OX** aqueous solution containing 0.2 M Na_2SO_4 (pH 2.1).

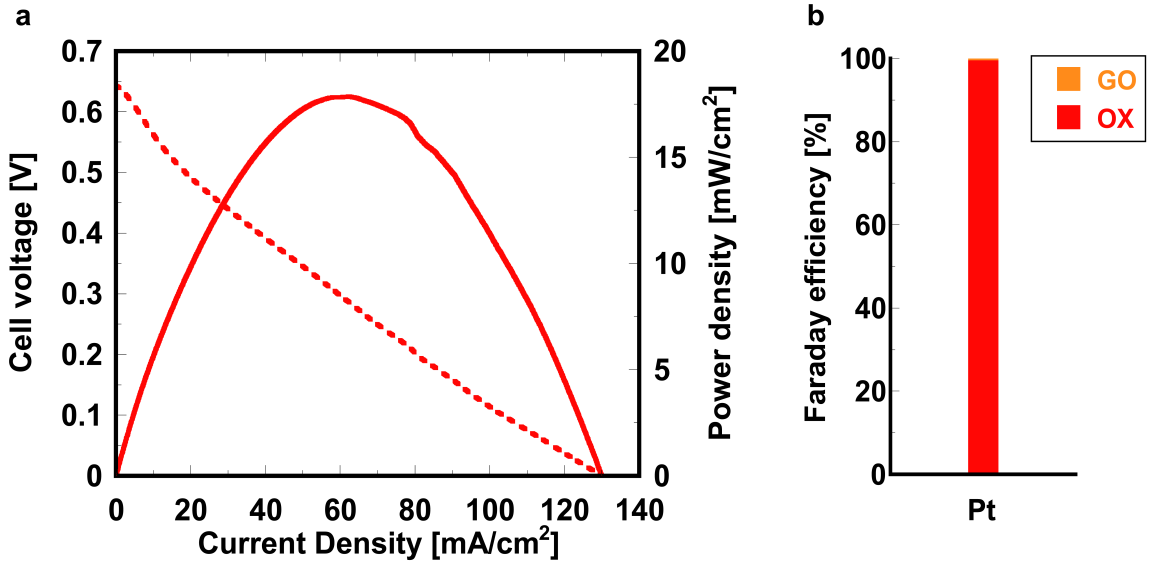

Fig. 4 Performance of a direct **GC**-AFC. (a) Potentiodynamic and power density curves of a direct **GC** alkaline fuel cell. The broken and solid lines indicate polarisation and power density curves, respectively. The fuel cell tests were performed by employing a commercial 20 wt.% Pt catalyst as an anode catalyst and $LaSr_3Fe_3O_{10}$ as an alkaline electrolyte with 10 wt.% **GC** and 10 wt.% KOH at a scan rate of 1 mA/s. (b) Faraday efficiency for **GC** oxidation products **OX** and GO in electrooxidation on the Pt catalyst.

Cyclic voltammetry (CV) indicated that the onset potentials of **OX** reduction on Ti foil, Ti foils modified with **PTS**-450, -500 and -600 were -0.28, -0.15, -0.11 and -0.25 V vs. RHE, corresponding to overpotentials of 0.41, 0.28, 0.24 and 0.38 V vs. RHE, respectively (Fig. S8). It is notable that the **PTS**-500-modified electrode exhibited the lowest overpotential and the largest reduction current. Recently, efficient hydrogen evolution by H_2O electrolysis at low overpotentials has been realised[41-48]. Given that the overpotentials for hydrogen evolution vary from 0.040 to 0.35 V vs. RHE, **GC** production via **OX** electroreduction is competitive with H_2O electrolysis. The temperature dependence of the catalytic performance of **PTS**-500 in 0.03 M **OX** with 0.2 M Na_2SO_4 at -0.7 V vs. RHE was investigated (Figs. 3(a), (b) and (c), and Figs. S9(a), (b) and (c)). **GC** selectivity was enhanced to 99% when the temperature was increased from 24 to 50 ºC, and 92-96% Faraday efficiencies were achieved at each reaction temperature. Considering that the electroreduction performed at 50 ºC exhibited the highest efficiency for **GC** formation (Fig. 3(c)), we examined the dependence of potential on **OX** reduction at 50 ºC (Figs. 3(d), (e) and (f), and Figs. S9(d), (e) and (f)). In the potential region of -0.4 to -0.6 V vs. RHE, the **GC** selectivity remained >98%, even after 6 h. Electroreductions performed at -0.5 and -0.6 V resulted in ca. 70 and 80% Faraday efficiencies, respectively, although the efficiency obtained at -0.4 V was 20%. Thus, even by employing an electrode simply fabricated via solvent evaporation, we achieved efficient **OX** reduction with >98% **GC** selectivity and 70-95% Faraday efficiency in the potential range of -0.5 to -0.7 V vs. RHE at 50 ºC. For the stability evaluation of the catalyst, repeated **OX** electroreductions using an identical electrode were performed. The **GC** selectivity and Faraday efficiency in **OX** reduction remained >98% and 80%, respectively, in three successive reactions using a **PTS**-500-modified electrode as shown in Fig. S10. Gradual exfoliations of the catalysts from the electrode were observed during the measurements. These results suggest that catalytic activities of **PTS**-500 are maintained under the conditions applied in this study and the observed deterioration in Faraday efficiency mainly comes from the exfoliation of **PTS**-500 from the Ti foil. Therefore, we believe that appropriate improvements in the electrode fabrication method will conduce to further enhancement in catalytic performances of **PTS**s.

We then demonstrated the feasibility of power generation by direct **GC** electrooxidation using alkaline fuel cells (direct **GC**-AFC). The potentiodynamic and power density curves obtained with 10 wt.% **GC** in 10 wt.% KOH at 70 ºC using a previously reported[20] alkaline fuel cell fabricated using $LaSr_3Fe_3O_{10}$ as an electrolyte are shown in Fig. 4(a). The cell employing a commercial Pt catalyst exhibited an open-circuit potential of 0.65 V and a peak power density of 18 mW/cm^2. Notably, 99% selectivity for **OX** formation and 100% Faraday efficiency were confirmed (Fig. 4(b)), which are requisites for realising CO_2-free power generation. We estimated efficiencies in the power charge and discharge processes by assuming 100% efficiency for both O_2 evolution and reduction on the Pt counter electrode using the method described in Supporting Information. The efficiencies for **OX** electroreduction at -0.6 V vs. RHE and **GC** electrooxidation at 0.6 V vs. RHE were determined to be 39 and 38%, respectively. These efficiencies will be enhanced by improvements in electrode structures.

Conclusions

We succeeded in **OX** electroreduction into **GC** on **PTS** catalysts, which is the first demonstration of direct electric power storage via electroreduction of a carboxylic acid. Catalytic performances of **PTS**s depended strongly on the calcination temperature in the catalyst preparation process. Detailed structural analyses including state-of-the-art EELS mappings attributed the highest activity of **PTS**-500 to energy states of a purely anatase-type TiO_2 and active surfaces formed on porous titanates. Furthermore, we performed power generation via highly selective electrooxidation of **GC** to **OX** without CO_2 emission using a direct **GC**-AFC with a Pt anode catalyst. This work presents the first experimental proof-of-concept of renewable electricity circulation using an alcohol/carboxylic acid redox couple with a minimal environmental impact. We believe that this novel idea for energy circulation will contribute to the efficient distribution of renewable electricity and to the realisation of a sustainable society.

Acknowledgements

The authors are grateful to Ms. Minako Heima and Mr. Eichi Arikawa for their help in electrochemical tests, and Mr. Takeshi Daio for his help in STEM-EELS measurements. This work was supported by JST-CREST and JSPS KAKENHI Grant Numbers 25288030 and 24655040.

Notes and references

[a] International Institute for Carbon Neutral Energy Research (WPI-I^{2}CNER), Kyushu University, Motooka 744, Nishi-ku, Fukuoka 819-0395, Japan.

[b] CREST, JST, 4-1-8 Honcho, Kawaguchi, Saitama 332-0012, Japan.

[c] Graduate School of Engineering, Kyoto University, Katsura, Nishikyo-ku, Kyoto 615-8510, Japan.

[d] Department of Chemistry and Bioengineering, Faculty of Engineering, Iwate University, 4-3-5 Ueda, Morioka, Iwate 020-8551, Japan.

† Electronic Supplementary Information (ESI) available: Experimental methods, Scheme S1 and S2, and Figs. S1 to S10 are given. See DOI: 10.1039/c000000x/

1 H. Chen, T. N. Cong, W. Yang, C. Tan, Y. Li, Y. Ding, *Prog. Nat. Sci.*, 2009, **19**, 291.
2 J. A. Turner, *Science*, 2004, **305**, 972.
3 M. Beaudin, H. Zareipour, A. Schellenberglabe, W. Rosehart, *Energy Sustain. Dev.*, 2010, **14**, 302.
4 K. Mazloomi, C. Gomes, *Renew. Sust. Energy Rev.*, 2012, **16**, 3024.
5 F. Barbir, Energy, 2009, **34**, 308.
6 M. Momirlan, T. N. Veziroglu, *Int. J. Hydrog. Energy*, 2005, **30**, 795.
7 L. Schlapbach, A. Züttel, *Nature*, 2001, **414**, 353.
8 C. J. Wnter, *Int. J. Hydrog. Energy*, 2009, **34**, S1.
9 H. K. Abdel-Aal, M. Sadik, M. Bassyouni, M. Shalabi, *Int. J. Hydrog. Energy*, 2005, **30**, 1511.
10 R. S. Irani, *MRS Bull*., 2002, **27**, 680.
11 J. Weitkamp, M. Frits, S. Ernst, *Int. J. Hydrog. Energy*, 1995, **20**, 967.
12 A. C. Dillon, K. M. Jones, T. A. Bekkedahl, C. H. Kiang, D. S. Bethune, M. J. Heben, *Nature*, 1997, **386**, 377.
13 J. L. C. Rowsell, O. M. Yaghi, *Angew. Chem. Int. Ed.*, 2005, **44**, 4670.
14 Y. Okada, E. Sasaki, E. Watanabe, S. Hyodo, H. Nishijima, *Int. J. Hydrog. Energy*, 2006, **31**, 1348.
15 J. F. Hull, Y. Himeda, W. H. Wang, B. Hashiguchi, R. Periana, D. J. Szalda, J. T. Muckerman, E. Fujita, *Nat. Chem.*, 2012, **4**, 383.
16 S. I. Orimo, Y. Nakamori, J. R. Eliseo, A. Züttel, C. M. Jensen, *Chem. Rev.*, 2007, **107**, 4111.
17 U. Eberle, M. Felderhoff, F. Schüth, *Angew. Chem. Int. Ed.*, 2009, **48**, 6608.
18 C. Bianchini, P. K. Shen, *Chem. Rev.*, 2009, **109**, 4183.
19 E. Antolini, *J. Power Sources*, 2007, **170**, 1.
20 T. Matsumoto, M. Sadakiyo, M. L. Ooi, S. Kitano, T. Yamamoto, S. Matsumura, K. Kato, T. Takeguchi, M. Yamauchi, *Sci. Rep.*, 2014, **4**, 6.
21 T. Yokoyama, T. Setoyama, N. Fujita, M. Nakajima, T. Maki, K. Fujii, *Appl. Catal. A-Gen.*, 1992, **88**, 149.
22 H. G. Manyar, C. Paun, R. Pilus, D. W. Rooney, J. M. Thompson, C. Hardacre, *Chem. Commun.*, 2010, **46**, 6279.
23 W. Rachmady, M. A. Vannice, *J. Catal.*, 2000, **192**, 322.
24 J. Xu, K. P. Sun, L. Zhang, Y. L. Ren, X. L. Xu, *Catal. Commun.*, 2005, **6**, 462.
25 G. Onyestyak, S. Harnos, S. Klebert, M. Stolcova, A. Kaszonyi, D. Kallo, *Appl. Catal. A-Gen.*, 2013, **464**, 313.
26 W. J. Li, L. M. Ye, P. Long, J. Chen, H. Ariga, K. Asakura, Y. Z. Yuan, *RSC Adv.*, 2014, **4**, 29072.
27 Z. Q. Wang, G. Y. Li, X. Y. Liu, Y. Q. Huang, A. Q. Wang, W. Chu, X. D. Wang, N. Li, *Catal. Commun.*, 2014, **43**, 38.
28 H. Olcay, L. J. Xu, Y. Xu, G. W. Huber, *ChemCatChem*, 2010, **2**, 1420.
29 J. M. Lee, P. P. Upare, J. S. Chang, Y. K. Hwang, J. H. Lee, D. W. Hwang, D. Y. Hong, S. H. Lee, M. G. Jeong, Y. D. Kim, Y. U. Kwon, *ChemSusChem*, 2014, **7**, 2998.
30 J. C. Serrano-Ruiz, A. Pineda, A. M. Balu, R. Luque, J. M. Campelo, A. A. Romero, J. M. Ramos-Fernández, *Catal. Today*, 2012, **195**, 162.
31 J. J. Xu, D. Xu, Z. L. Wang, H. G. Wang, L. L. Zhang, X. B. Zhang, *Angew. Chem. Int. Ed.*, 2013, **52**, 3887.
32 L. Zhang, K. Lee, J. J. Zhang, *Electrochim. Acta*, 2007, **52**, 3088.
33 H. B. Wu, X. W. D. Lou, H. H. Hng, *Chem. Eur. J.*, 2012, **18**, 2094.
34 H. Jensen, A. Soloviev, Z. S. Li, E. G. Søgaard, *Appl. Surf. Sci.*, 2005, **246**, 239.
35 F. De La Peña, M. –H. Berger, J. –F. Hochepied, F. Dynys, O. Stephan, M. Walls, *Ultramicroscopy*, 2011, **111**, 169.
36 T. Torimoto, N. Nakamura, S. Ikeda, B. Ohtani, Phys. *Chem. Chem. Phys.*, 2002, **4**, 5910.
37 D. Vesudevan, P. N. Anantharaman, *J. Appl. Electrochem.*, 1994, **24**, 559.
38 F. M. Zhao, F. Yan, Y. Qian, Y. H. Xu, C. Ma, *J. Electroanal. Chem.*, 2013, **698**, 31.
39 D. Chu, M. Xu, J. Lu, P. Zheng, G. Qin, X. Yuan, *Electrochem. Commun.*, 2008, **10**, 350.
40 R. Wang, K. Hashimoto, A. Fujishima, M. Chikuni, E. Kojima, A. Kitamura, M. Shimohigoshi, T. Watanabe, *Nature*, 1997, **388**, 431.
41 B. F. Cao, G. M. Veith, J. C. Neuefeind, R. R. Adzic, P. G. Khalifah, *J. Am. Chem. Soc.*, 2013, **135**, 19186.
42 Q. Liu, J. Q. Tian, W. Cui, P. Jiang, N. Y. Cheng, A. M. Asiri, X. P. Sun, *Angew. Chem. Int. Ed.*, 2014, **53**, 6710.
43 J. Q. Tian, Q. Liu, N. Y. Cheng, A. M. Asiri, X. P. Sun, *Angew. Chem. Int. Ed.*, 2014, **53**, 9577.
44 J. Kibsgaard, Z. B. Chen, B. N. Reinecke, T. F. Jaramillo, *Nat. Mater.*, 2012, **11**, 963.
45 M. A. Lukowski, A. S. Daniel, F. Meng, A. Forticaux, L. S. Li, S. Jin, *J. Am. Chem. Soc.*, 2013, **135**, 10274.
46 J. F. Xie, H. Zhang, S. Li, R. X. Wang, X. Sun, M. Zhou, J. F. Zhou, X. W. Lou, Y. Xie, *Adv. Mater.*, 2013, **25**, 5807.
47 E. S. Andreiadis, P. A. Jacques, P. D. Tran, A. Leyris, M. Chavarot-Kerlidou, B. Jousselme, M. Matheron, J. Pecaut, S. Palacin, M. Fontecave, V. Artero, *Nat. Chem.*, 2013, **5**, 48.
48 D. Voiry, H. Yamaguchi, J. W. Li, R. Silva, D. C. B. Alves, T. Fujita, M. W. Chen, T. Asefa, V. B. Shenoy, G. Eda, M. Chhowalla, *Nat. Mater.*, 2013, **12**, 850.

TOC Sentence:

We demonstrate a carbon-neutral energy circulation by highly selective electrocatalyses using the glycolic acid/oxalic acid redox couple.

Broader context:

An excessive increase of CO_2 in the atmosphere is regarded as the most probable cause of global warming. A substantive transition from fossil-based systems to systems operated by electricity that is generated using renewable energy, i.e., “renewable electricity”, seems to be the optimal answer to this environmental issue. A lack of efficient distribution techniques for unstably supplied and unevenly distributed renewable electricity is one of the fundamental impediments to its practical use. Thus, electric power storage in high-energy chemicals, called “energy carriers”, has received much attention for the efficient storage and on-demand supply of renewable electricity. Here, we demonstrate direct electric power charge using an alcohol/carboxylic acid redox couple. Highly energetic and transportable glycolic acid, an alcoholic compound, was successfully produced by electroreduction of oxalic acid, a dicarboxylic acid, on ubiquitous TiO_2 catalysts with high efficiency and selectivity (70-95% Faraday efficiency and >98% selectivity). Furthermore, we succeeded in electric power generation via the selective electrooxidation of glycolic acid to oxalic acid without CO_2 emission—specifically, carbon-neutral power generation. These results are the first experimental proof of concept for a carbon-neutral energy circulation system based on charging/discharging electric power using an alcohol/carboxylic acid redox couple.